An automatic graph-based method for characterizing multichannel networks

Yanhui Liu[a,b,e], Paul A. Carling[b,c,d], Yuanjian Wang[a], Enhui Jiang[a], Peter M. Atkinson[b,c,f,*]

[a] *Yellow River Institute of Hydraulic Research, Zhengzhou 450003, China*
[b] *Lancaster Environment Centre, Lancaster University, Bailrigg, Lancaster LA1 4YR, UK*
[c] *Geography and Environmental Science, University of Southampton, Highfield, Southampton SO17 1BJ, UK*
[d] *State Key Laboratory of Geohazard Prevention and Geoenvironment Protection, Chengdu University of Technology, Chengdu, Sichuan 610059, China*
[e] *College of Water Conservancy and Hydropower Engineering, Hohai University, Nanjing 210098, China*
[f] *Institute of Geographic Sciences and Natural Resources Research, Chinese Academy of Sciences, 11A Datun Road, Beijing 100101, China*

ABSTRACT: Assessment and quantitative description of river morphology using widely recognized river planview measures (*e.g.*, length, width and sinuosity of channels, bifurcation angles and island shape) for multichannel rivers are regarded as fundamental parts of the toolkit of geomorphologists and river engineers. However, conventional assessment methods including field surveys or exiting algorithms for the extraction of multichannel planviews might be suboptimal. More recently, the potential for the application of complex network analysis to the study of river morphology has led to emphasis on the accurate characterization and definition of multichannel network topology. Therefore, we developed a novel algorithm called RivMACNet (River Morphological Analysis based on Complex Networks) that enables the extraction of multichannel network topology using satellite sensor images as the input. We applied RivMACNet to a meandering reach of the Yangtze River and a strongly anastomosing reach of the Indus River to construct their network

* Corresponding author. Lancaster Environment Centre, Lancaster University, Bailrigg, Lancaster LA1 4YR, UK
E-mail address: pma@lancaster.ac.uk (Peter M. Atkinson)

topologies, and then calculated a series of common topological measures including weighted degree (WD), clustering coefficient (CC) and weighted characteristic path length (WCPL). The network analysis indicated that both networks exhibit poor transitivity with small clustering coefficients. The topological properties of the Indus at the reach scale are independent of flow conditions, while they vary across space at the subnetwork scale. In addition, comparison between RivMACNet and an alternative common river network analysis engine (RivaMap) demonstrated that RivMACNet is superior in terms of representation accuracy and network connectivity and, thus, is more suitable for multichannel fluvial systems with complex planviews. RivMACNet is, thus, a useful tool to support further investigation of multichannel river networks using graph theory.

Keywords: multichannel network, remote sensing, complex network analysis, river network topology, graph theory.

1. Introduction

Fluvial systems are generally regarded as linear features that can be divided into two distinct groups based on current river channel classification patterns (Nanson and Knighton, 1996): (i) single channel networks such as straight rivers and meandering rivers (Parker et al., 2011), and (ii) multichannel networks (Carling et al., 2014) defined as river planviews composed of more than one interlinked channel forming inosculate patterns, such as braiding and anabranching rivers (Leopold and Wolman, 1957; Parker 1976; Rust, 1978; Bridge 2009; Jansen and Nanson, 2010; Meshkova and Carling, 2013; Kleinhans et al., 2019; Hiatt et al., 2020). The largest rivers on Earth often exhibit a network of multiple channels and, thus, can be regarded as naturally occurring forms of a generic class of network structures (Gupta, 2008). Different channel planforms are thought to reflect differences in river behaviour, and planform assessment remains central to all modern river channel classification schemes (Carling et al., 2014). However, quantitative assessment of river planviews is considered a challenging task in river channel analyses, inclusive of channel evolution, migration and bank erosion (Miller, 1988; Osman and Thorne, 1988; Richardson, 2002; Smith and Pain, 2009; Kleinhans et al., 2013; Grabowski et al., 2014; Yousefi et al., 2016; Li et al., 2017; Shahrood et al., 2020).

For over half a century, researchers have quantified different elements of channel planviews via metrics including the braiding index, bifurcation angle, channel width, length, sinuosity and migration distance, as well as island and sand bar shapes (Parker and Anderson, 1975; van den Berg, 1995; Chew and Ashmore, 2001; Tooth and Nanson, 2004; Xu, 2004; Harrison et al., 2011;

Shwenk, 2016; Ashour et al., 2017; Yukawa et al., 2019; Liu et al., 2021). However, such conventional quantitative geometrical metrics of fluvial systems are unlikely to be sufficient to define, or discriminate between, channel types (Carling et al., 2014). Meanwhile, the definition of river network topologies (Dodds and Rothman, 2000; Rodriguez and Rinaldo, 2000) and their stream ordering laws (Tokunaga, 1966; Williams and Rust, 1969; Bai et al., 2015) demonstrates that river networks can be treated as real-world, non-random networks of varying complexity. In this view, channel bifurcations (whether divergent or convergent) are nodes, with the individual channels between nodes regarded as links. With the development of complex network analysis (Watts and Strogatz, 1998; Newman, 2003; Rubinov and Sporns, 2010), the topological properties of multichannel networks, which could highlight emergent and novel spatial and temporal relations at some local or reach scales for river channels, have attracted interest from researchers. Despite some success in the quantification of river network topology and some common topological measures such as Betweenness Centrality (BC) (Marra et al., 2014), physical or hydraulic explanations for such topological properties within multichannel networks have been limited. One reason is that no efficient tools were proposed for multichannel network construction and the subsequent extraction of a range of potentially useful metrics including both geometrical and topological measures.

Conventional field surveys and manual inspections of remote sensing images are prohibitively expensive and laborious for defining and constructing multichannel topologies and are subject to operator errors (Gupta et al, 2013; Guo et al., 2017). Increasingly, developments in remote sensing and image processing provide the possibility of reliable automated algorithms or software packages to extract some of the aforementioned river networks. Examples include: RivWidth (Pavelsky and Smith, 2008) and RivaMap for river width (Isikdogan et al., 2017); PyRIS (Monegaglia et al., 2018) and RiMARS for river network morphology analysis (Shahrood et al., 2020); and RovMAP for river migration (Schwenk, 2016), as well as other methods for constructing the topology of river networks (Chen et al., 2019; Schwenk and Hariharan, 2021). However, gaps remain in terms of methods for the construction of river network representations, especially for multichannel networks as follows: (i) most methods adopt a channel mask that differentiates those areas that are within the river boundary (including islands or sand bars) and those areas outside the river boundary (Pavelsky and Smith, 2008), but ignore islands or sand bars located within rivers, which is unacceptable for multichannel networks as island presence and shape plays an important role in defining multichannel networks (Meshkova and Carling, 2013); (ii) it is difficult to guarantee the connectivity of the output river channels when the method for delineating the river network relies on centerlines (Shahrood et al., 2020) and, thus, such methods result in extra bifurcation nodes and links being identified, and; (iii) geometrical measures of individual channels including length, width, and sinuosity are poorly quantified during the process of multichannel network construction (Chen et al., 2019), such that whether the river network topology is related to river behaviour remains unknown.

The objectives of the research reported herein were to develop a novel river morphological analysis method based on complex networks, called RivMACNet, for multichannel topology construction and assessment, as well as extraction of a range of geometrical and topological measures. The remainder of this paper is organized as follows. In section 2, the algorithms and methods used in RivMACNet and some common topological and geometrical measures of multichannel networks are introduced. Section 3 presents two selected study reaches, part of the Yangtze and Indus multichannel networks. Section 4 presents the results of the case study in detail including its topological and geometrical measures at the reach and sub-network scales, in which RivMACNet is tested and validated. In section 5, we discuss the advantages of RivMACNet for quantifying multichannel networks by comparing RivMACNet with another conventional method: RivaMap. Section 6 ends the paper with a conclusion.

2. Methods

2.1 River network topology construction

The general methodology for constructing a river network topology using remote sensing comprises the following steps: (i) water body extraction; (ii) river channel delineation; (iii) node detection; and, (iv) derivation of the river network connectivity matrix (Chen, 2019). Each of these steps in RivMACNet is introduced systematically in this section, with particular attention given to improvements over conventional methods and algorithms. Our proposed software tools were developed in MATLAB, and are freely available at: http://github.com/lyh444/ RivMACN.git.

Water body extraction: Various reliable algorithms and methods can be used for extracting singular objects like rivers from remote sensing images (McFeeters, 1996; Xu, 2006; Petropoulos et al, 2012; Zhu et al., 2015). In RivMACNet, we employed a widely accepted index called the Modified

Normalized Difference Water Index (MNDWI) (Xu, 2006) to extract the water bodies, which can be expressed as follows:

$$\text{MNDWI}=\frac{\text{Green-MIR}}{\text{Green+MIR}}, \tag{1}$$

where Green is a green band, such as band 2 for Landsat 5, while MIR is a middle infrared band, such as band 5 for Landsat 5. Water bodies have greater positive MNDWI values, so that a simple thresholding method (the threshold is 0 in this paper unless otherwise stated) can be used for extraction. In this manner, the extracted water bodies (Fig. 1B) are represented by a binary image: 1 (river network pixels) and 0 (background pixels). However, although sporadic discrete water bodies like ponds, lakes, and isolated channels (these are correctly classified as water, but are not of interest) can be removed by saving only the largest portion of the extracted water bodies, some remaining noise is inevitable, particularly in a group of misclassified pixels which we refer to as small 'background holes' located in the river channel (*e.g.*, false sand bars or island objects caused by bridges or rivercraft) (Fig. 1C). Such noise cannot actually affect the river morphology, but can lead to discontinuity in the river topology or the miscounting of bifurcations and channels. To fill these holes within the extracted water bodies, we apply a convolutional filter window to the entire binary image. This window, shown in Fig. 2A, employs a variable size σ (σ=3, 5, 7…) with edge pixels set to 1 and the rest 0. For background pixels, if the convolution results are equal to (4σ-4), they are recorded as 'holes' that need to be filled. The size of the convolution kernel is increased gradually and the above steps are repeated. In this manner, the final river network with noise removed can be derived (Fig. 1D).

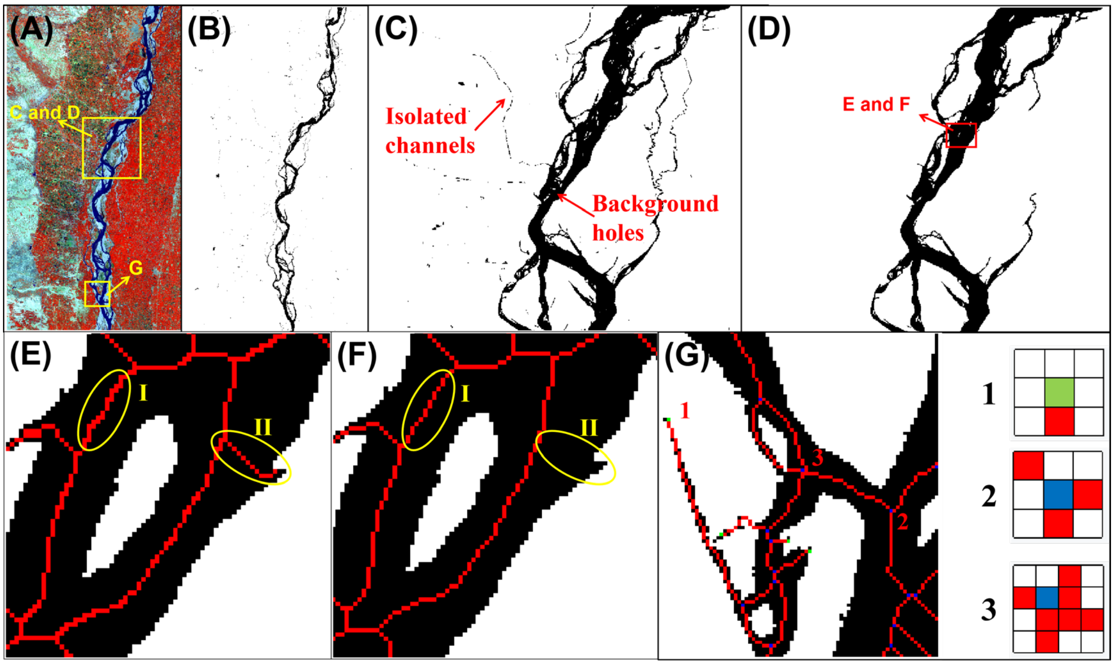

Fig. 1. (A) false colour composite of Landsat 5 TM image derived from Indus River in Pakistan. (B) water bodies extracted in (A) based on *MNDWI*. (C) zoomed image of (B). (D) water bodies without noise after the process of noise elimination in (C). (E) and (F) comparison of thinning results: (E) original Zhang-Suen algorithms and (F) the revised algorithms in RivMACNet. Red pixels represent channel skeletons. (G) illustration of the node detection in RivMACNet. Nodes 1, 2 and 3 are examples of end nodes (green pixels) and bifurcation nodes (blue pixels) with different patterns in (G), respectively.

Delineating the river channels: The aforementioned water bodies are usually reduced to a set of single-resolution lines (herein termed 'river representatives') to define the links and nodes in the multichannel network (Schaefer and Pelletier, 2020). In contrast to conventional river representations such as geometrical channel centerlines (EGIS, 2002; Mount et al., 2003), river skeletons (Hasthorpe and Mount, 2007) are defined as the refined curves with the same geometrical characteristics as the river channels. This approach has the advantage of maintaining the connectivity of the refined curves and greater enforcement efficiency (Shen et al., 2017; Chen et al., 2019). We adopt the revised version of the classic Zhang-Suen fast parallel thinning algorithm presented by Chen et al. (2012) in RivMACNet to produce one-pixel wide river skeletons (*e.g.*, I in Fig.1F). This procedure avoids unwanted spurs caused by local convex water pixels (*e.g.*, II in Fig. 1E) in contrast to the original algorithm (Zhang and Suen, 1984).

Node detection: The river skeleton image is convolved with a mask for node detection in RivMACNet. The conventional method (Olsen et al., 2011), using a simple 3×3 mask (Fig. 2B), can detect only eight end nodes and 18 bifurcation node structures (*e.g.*, node 1 and 2 in Fig. 1G) in river skeletons, but ignores the structure formed by two adjacent bifurcation nodes (and one node connecting four or more links) due to the limitation of the mask size (*e.g.*, node 3 in Fig. 1G). A higher order 4×4 mask with a 2×2 sub-window (Fig. 2B) is added in RivMACNet to detect the remainder of the nodes because of the extendibility of the method. Each skeleton pixel within the image is traversed using the 3×3 mask and 4×4 mask, in turn. The former mask has 1 center pixel P_i (i = 1) and 8 edge pixels P_j (j = 2, 3, ..., 9), while the latter has 4 center pixels P_i (i = 1, 2, 3, 4) and 12 edge pixels P_j (j = 5, 6, ..., 16). Center pixels and edge pixels in both masks are all sorted clockwise (Fig. 2B). Pixels satisfying the following conditions are defined as end or bifurcation nodes:

$$\mathrm{P} \in \begin{cases} \text{end node,} & \text{if } N_p\text{=1 and } N_s\text{=1;} \\ \text{bifurcation node connecting to 3 links,} & \text{if } N_p\text{=1 and } N_s\text{=3;} \\ \text{bifurcation node connecting to more than 3 links,} & \text{if } N_p > 2 \text{ and } N_s > 3; \end{cases} \quad (2)$$

where N_s and N_p are defined as the number of edge pixels P_j and middle pixels P_i within two masks that belong to skeletons (Fig. 2B). In addition, RivMACNet omits the node structures where an individual channel ends with a bend (e.g., Fig. 2C): N_p = 1, N_s = 2. Such output would not be generated by the thinning algorithm, as it would be further refined into a single pixel-wide end node skeleton.

In the above manner, all detected nodes can be recorded as the node matrix **Node** = {X_i, Y_i} (X_i and Y_i are the pixel coordinates of the i-th node in water body binary images), where nodes are sorted in order from upstream to downstream within the multichannel network according to the Euclidean distances between them and the start point of the multichannel centerline (see Fig. 4A). The order of nodes in connectivity matrices has no effect on the computation of network measures (Rubinov and Sporns, 2010). Specifically, for two nodes i and j with the same distance from the start of the channel network, $i < j$ when (i) $X_i < X_j$, or (ii) $Y_i < Y_j$ if $X_i = X_j$.(Fig. 4A)

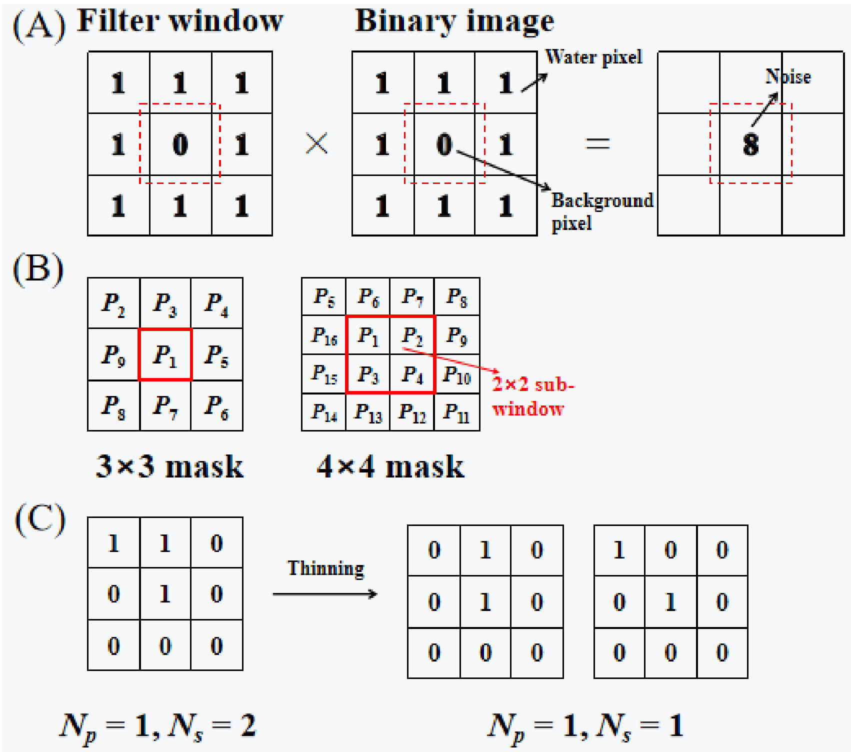

Fig. 2. (A) illustration of the convolution between the filter window structure (take $\sigma = 3$ as an example) and binary images. (B) two node detection masks with different sizes. (C) examples of end node structures: (left) $N_p = 1$, $N_s = 2$; (right) $N_p = 1$, $N_s = 1$.

<u>Derivation of the river network connectivity matrix</u>: the connectivity matrix **A**={$a_{i,j}$} shown in Fig. 3B plays an important role in the calculation of river network topological measures (Rubinov and Sporns, 2010). Its rows and columns denote nodes, while matrix entries denote links. $a_{i,j}$ = 1 if node i is

connected to node *j*, while 0 if they are not connected. A tracking algorithm from one node to another was presented in RivMACNet to construct the river network topology automatically, summarized as follows:

(i) Define the zero matrix **A**=$\{a_{i,j}\}_{n\times n}$ (*n* is the node numbers) and traverse each detected node in the **Node** matrix.

(ii) Take node *i* as the starting pixel and track each skeleton connecting to node *i* by pixels, in turn, until another node *j* at the other side of the skeleton is reached. Then, $a_{i,j}=a_{i,j}+1$. If all skeletons connecting to *i* have been tracked, then move to the next node pixel (Fig. 3B).

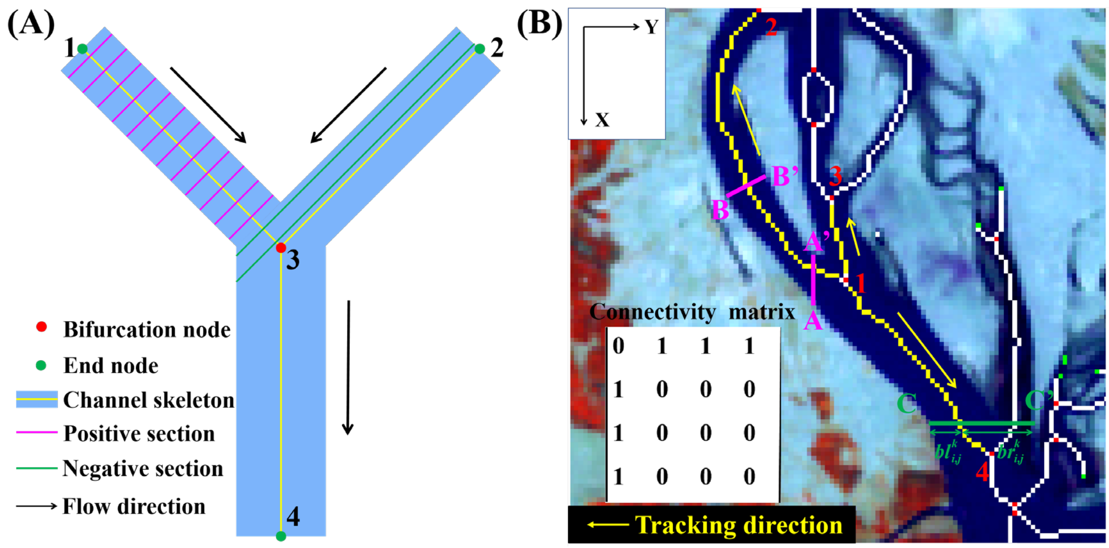

Fig. 3 (A) Examples of the positive and negative cross-sections in a 4-node multichannel network. (B) Illustration of the tracking process from node 1 to others (nodes 2 - to - 4) as well as their connectivity matrix. Red numbers represent nodes, while magenta and green lines are positive and negative cross-sections located on the individual channels, respectively. The value of the pixel coordinate *X* increases in the downstream direction of the river network in RivMACNet.

2.2 Channel planview measures

Two groups of channel planview measures including geometrical and topological properties of multichannel networks are introduced in this section. RivMACNet establishes the bridge between such geometrical and topological measures to provide certain physical and hydraulic bases for complex network analysis of multichannel networks. The extraction process of channel geometrical measures in the multichannel network actually occurs during the tracing from one node *i* to another node *j* in the river network.

Two kinds of channel length are considered in RivMACNet: the curve length $l^{c}_{i,j}$ and the straight line distance $l^{s}_{i,j}$ of the individual channel between two consecutive bifurcations *i* and *j*, which can be expressed as follows:

$$l^{c}_{i,j} = IR \times \sum_{k=1}^{K} \sqrt{(X^{k+1}_{i,j}-X^{k}_{i,j})^{2}+(Y^{k+1}_{i,j}-Y^{k}_{i,j})^{2}}, \tag{3}$$

$$l^{s}_{i,j} = IR \times \sqrt{(X_i-X_j)^{2}+(Y_i-Y_j)^{2}}, \tag{4}$$

where $X^{k}_{i,j}$ and $Y^{k}_{i,j}$ are the (X, Y) location coordinates of the *k-th* pixel in the skeleton connecting nodes *i* and *j*, while *K* is the total pixel number of the skeleton, and *IR* (in units of m) indicates the image resolution.

Channel sinuosity $s_{i,j}$ can be defined as the ratio of the aforementioned two kinds of lengths of the corresponding skeleton connecting nodes *i* and *j*:

$$s_{i,j} = \frac{l^{c}_{i,j}}{l^{s}_{i,j}}. \tag{5}$$

The individual channel width could be considered equal to the mean lengths of a set of measurement cross-sections (Fig. 3A) (Howard et al., 1970) separated by approximately equal distance (spaced one pixel apart in this paper) along its skeleton. Each cross-section is set orthogonal to the local orientation of the channel skeleton in RivMACNet:

$$slop^{k}_{i,j} = \frac{Y^{k+1}_{i,j}-Y^{k-1}_{i,j}}{X^{k+1}_{i,j}-X^{k-1}_{i,j}}, \tag{6}$$

where $slop^{k}_{i,j}$ is the local orientation of the channel skeleton connecting nodes *i* and *j* at the *k*-th pixel. A special case is $X^{k+1}_{i,j} = X^{k-1}_{i,j}$, in other words, the denominator is zero. In this case, the orientation of the corresponding cross-section line is set to vertical in RivMACNet (e.g., A-A' in Fig. 3B).

However, not all cross-sections contribute when calculating the individual channel width, especially those near nodes. For example, the green sections in Fig. 3A measure not only the width of the individual channel connecting nodes 1 and 3, but also the length of the individual channel connecting nodes 2 and 3. Such cross-sections affected by other individual channels are defined as 'negative sections' and, thus, omitted in RivMACNet when calculating the channel width. Conversely, the 'positive sections' are roughly bisected by channel skeletons (e.g., B-B' in Fig. 3B), playing an important role in measuring channel widths. In this context, another coefficient called width gate Δb was introduced to distinguish between 'positive and negative sections'. The cross-section that intersects the k-th pixel of the channel skeleton connecting nodes i and j belongs to the 'positive section' when the following condition is true:

$$\Delta b \geqslant \left| bl_{i,j}^{k} - br_{i,j}^{k} \right|, \tag{7}$$

where $bl_{i,j}^{k}$ and $br_{i,j}^{k}$ represent lengths of the left and right sub-sections (e.g., C - C' in Fig. 3B) divided by the channel skeleton, respectively. As a result, the width $b_{i,j}$ of the individual channel connecting to nodes i and j is calculated as follows:

$$b_{i,j} = \frac{1}{K'} \sum_{k=1}^{K'} b_{i,j}^{k}, \tag{8}$$

where K' is the total number of the 'positive sections' located on the channel skeleton, while $b_{i,j}^{k}$ represent the length of the cross-section that intersects k-th skeleton pixel of the skeleton.

RivMACNet also highlights the calculation of common river network topological properties (Table 1), including degree, clustering coefficient, and the characteristic path length, based on the connectivity matrix **A** (Rubinov and Sporns, 2010).

Table1 Expressions of multichannel network topological measures

Measure	Unweighted expression[a]	Weighted expression[b]
Degree	$k_i = \sum_{j=1}^{n} a_{i,j}$	$k_i^w = \sum_{j=1}^{n} w_{i,j}^k$
Average neighbour degree[c]	$k_{nn,i} = \frac{\sum_{j=1}^{n} \alpha k_j}{k_i}$	$k_{nn,i}^w = \frac{\sum_{j=1}^{n} \alpha k_j^w}{k_i^w}$
Cluster coefficient	$C_i = \frac{\sum_{j,h \in n} a_{ij} a_{ih} a_{jh}}{k_i(k_i\text{-}1)}$	/
The characteristic path length[d]	$l = \frac{1}{\frac{1}{2}n(n+1)} \sum_{i \geq j} d_{i,j}$	$l^w = \frac{1}{\frac{1}{2}n(n+1)} \sum_{i \geq j} w_{i,j}^l$

[a]. a_{ij} represents values in the connectivity matrix A, while n is the total number of nodes.
[b]. $w_{i,j}^k$ and $w_{i,j}^l$ are weights for degree and the characteristic path length, respectively.
[c]. α is 1 if node i and j are neighbours, or 0 if they are not connected.
[d]. The characteristic path length of the network in RivMANCnet is calculated using the Floyd-Warshall (1962) algorithm.

In a river network, the degree k_i quantifies how many individual channels are connected to the bifurcation node i (divergent or convergent), while mean neighbour degree $k_{i,nn}$ measures the mean number of individual channels connecting to its neighbour nodes. In this manner, nodes within river networks can be divided roughly into three types (Fig. 4): (i) 'end nodes' ($k_i = 1$) indicate the upstream inlet and the downstream outlet of the river network as well the terminations of other channels; (ii) 'simple bifurcation nodes' ($k_i > 1$ and $k_{i,nn} < 3$) indicate divergent or convergent points because of the inflow and outflow of other streams; (iii) 'island or sand bar nodes' ($k_i > 1$ and $k_{i,nn} \geq 3$) indicate divergent or convergent points caused by enclosing sand bars or islands located in the river network.

Given the topological structure of the network there could be a probability that node *i* is connected to node *j* if both of them are neighbours of node *k*, a condition termed transitivity, or clustering of the network (Newman, 2003). The clustering coefficient C_i of node *i* (Table 1) is defined to quantify this neighbourhood property based on the ratio of the number of triangles (formed by islands and sand bars) and triples around node *i* (Fig. 4C). Specifically, C_i lies in the range [0, 1], with the maximum value of 1 if nodes in the river network connect to each other.

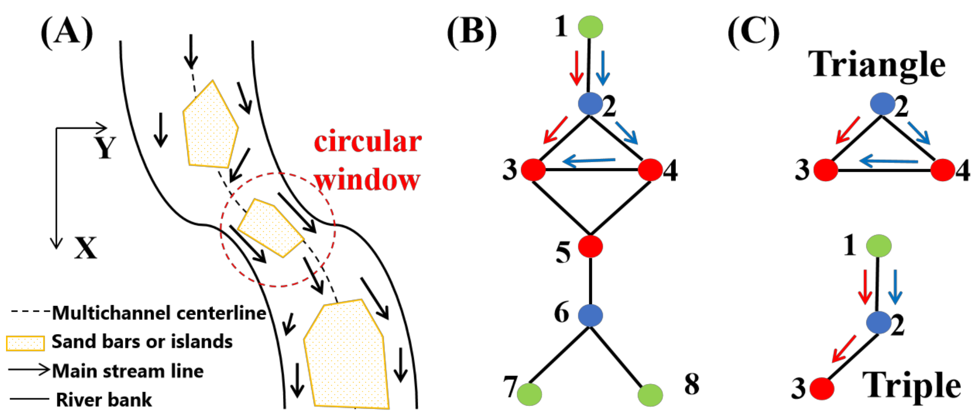

Fig. 4. (A) basic elements for multichannel networks, and red circle indicates circle raster for assessment of the network topology at a sub-network scale. (B) illustration of a river network topology in (A). Arrows indicate the flow orientation, while green, blue and red nodes indicate end, simple bifurcation and island/sand bar nodes, respectively. Two different paths from node 1 to 3 are showed by red, and blue arrows, respectively. (C) illustration of the 'triangle' around node 2 and the 'triple' structure centered on node 2 in (B). Node 2 has one triangle and three triples and, thus, its clustering coefficient is 1/3.

For multichannel networks, water and sediment could be transported from one node *i* to another *j* though different paths (*e.g.*, the two paths from node 1 to node 3 in Fig. 4B). Therefore, the characteristic path length *l* is defined as the mean value of the shortest path length $d_{i,j}$ between all pairs of nodes though the multichannel network. *l* is a connectivity measure of the multichannel network, and its minimum value is 1 if all divergent or convergent points connect to each other.

Multichannel networks are hydraulically complex and, thus, the aforementioned unweighted (channel links are equivalent in network analysis) topological properties cannot be related adequately to the controlling processes and variables of river channels. For example, the longitudinal slope, bankfull discharge, channel depth, and median diameter of bed material usually are unknown when interrogating remote-sensing images and these are widely considered to be important parameters in determining channel form and behaviour. However, link width and length often are considered to be related to bankfull discharge and channel slope, respectively, and bifurcation angles reflect well-studied hydrodynamic controls as well as the constraints imposed by the width of the macrochannel. In this context, the multichannel network topological properties were weighted in this paper to reflect unmeasured controls such as a slope and depth (Table 1). The weight for degree $w_{i,j}^{k}$ is the ratio of individual channel width and length, indicating that nodes with a larger weighted degree play a more important role in multichannel networks because they participate in more water and sediment transport and redistribution, while the weight for characteristic path length $w_{i,j}^{l}$ is the ratio of the length of the individual channel and the mean length of all channel links and is, thus, proportional to spatial distances for water and sediment transport. Additionally, no weight was set for the clustering coefficient, which is a density measure for the occurrence of sand bars and islands in multichannel networks. Expressions for these topological measures of unweighted and weighted multichannel networks are listed in Table 1.

2.3 Spatial evolution of topological measures at the sub-network scale

The planviews of multichannel networks vary due to the influence of upstream flow and boundary conditions. In addition to assessment of the global network properties, RivMACNet also provides methods to explore the spatial distributions of topological properties along the multichannel centerline by using a circular moving window (Fig. 4A) with an adjustable radius *R* instead of the macrochannel (van Niekerk et al., 1995) cross lines. In this manner, the local topological measures $f(x_0)$ at x_0 km from the most upstream extent of the multichannel network can be expressed as follows:

$$f(x_0)= \frac{1}{n_x}\sum f(x)_i, \tag{9}$$

where n_x is the total number of nodes in the circlular window, while $f(x)_i$ is the measure value of the *i*-th node.

3. Study area

To test the practical utility and reliability of RivMACNet, we selected two regions as study areas. Region I: the Yangtze River (Chen et al., 2019) near Wuhan, China (Fig. 5A); Region II: the Indus River (Inam et al., 2007; Ali, 2013; Syvitski and Brackenridge, 2013; Kale, 2014; Carling et al., 2018) between the Chashma and Taunsa barrages located in the middle of the Indus Basin in Pakistan (Fig. 5B). The former case is a meandering river reach, while the latter exhibits an anastomosed river pattern composed of sand bars, islands, wet channels, and dry channels.

Landsat 5/8 TM images of the two study reaches with a spatial resolution of 30/15 m were downloaded from Earth Explorer (http://earthexplorer.usgs.gov). The MNDWI was calculated for each of the pixels within the images, for use as the input to the RivMACNet algorithm. We selected three images to test our model. The first is the Landsat 8 TM image of

Region I in April 2019 with a size of 2705×1792 pixels. The other two are Landsat 5 TM images of Region II representing the low flow (LF) period in March 2011 and the high flow (HF) period in October 2011, to illustrate the reliability of the proposed method for identifying the river network topology between different flow conditions. Both images are 3000×3000 pixels. The ground data on water bodies were derived from the corresponding false colour composite of Landsat TM images by supervised classification using the support vector machine (SVM), which was executed in ENVI (Oliver, 2008). The training samples for each class were selected manually based on their colours. Although some error might be associated with the ground data, these data can be considered as a control group of constructed river channels when comparing RivMACNet with other methods because the error in the ground data is small relatively (Chen et al, 2019).

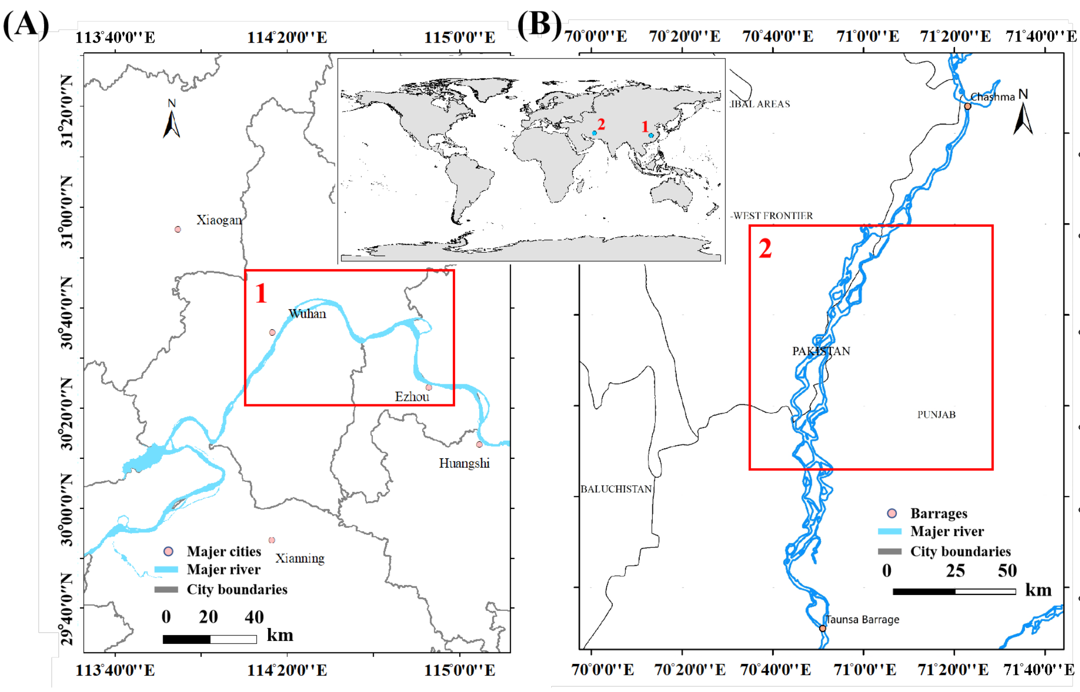

Fig. 5. Maps of the study river reaches on (A) the Yangtze River near Wuhan, and (B) the Indus River located between the Chashma and Taunsa barrages, Pakistan.

4. Results

4.1 Parameter settings

Before presenting results for the river network topologies and geometrical properties, essential parameter settings including the size of the noise removal window σ and the threshold of the width gate Δb need to be considered because different parameter values will lead to variable outputs. We set these parameters using data of the Indus. A larger σ makes RivMACNet insensitive to islands and sand bars. Fig. 6 illustrates the numbers of individual channels detected in the Indus network with different σ values during low and high flow periods, respectively. We tested different σ values and found that the output of individual channel numbers per macrochannel cross-section (m_{pc}) when σ = 7 is consistent with observation (by visual interpretation) that the Indus network has a minimum of two ($m_{pc,min}$ = 2) and a maximum of nine ($m_{pc,max}$ = 9) channels (Carling et al., 2018). Furthermore, the choice of threshold of Δb is a trade-off between the width-extraction accuracy and the number of individual channels. Thus, we employed a sensitivity analysis to determine its optimal value (Fig. 7). In Fig. 7, although a smaller threshold can strictly guarantee the accuracy of the detected river width it leads to the loss of channels. The latter phenomenon gradually improved as the threshold increased, and became stable at the threshold of Δb larger than 2. In this context, we set the threshold of Δb to 3 indicating that this optimal value can not only achieve a high measurement accuracy of the channel width, but also maximize the number of channels with positive width. We set the parameters to the aforementioned recommended values in all experiments reported in this paper.

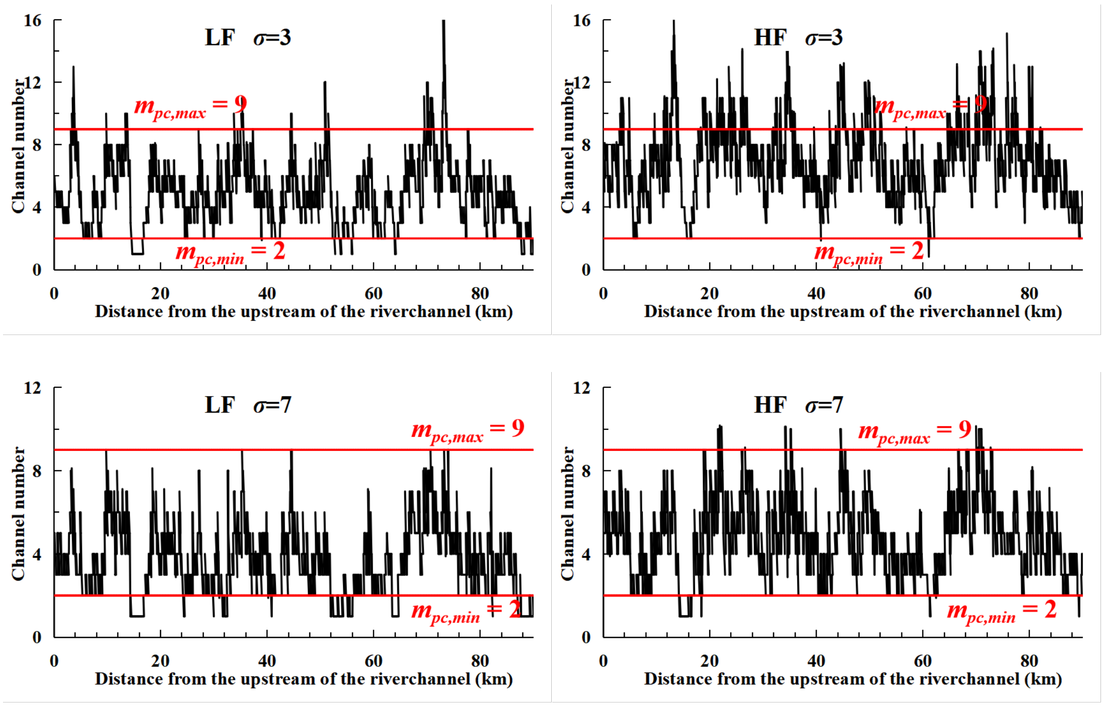

Fig. 6. Numbers of individual channels detected in the Indus network using different σ values during high flow (HF) and low flow (LF) periods.

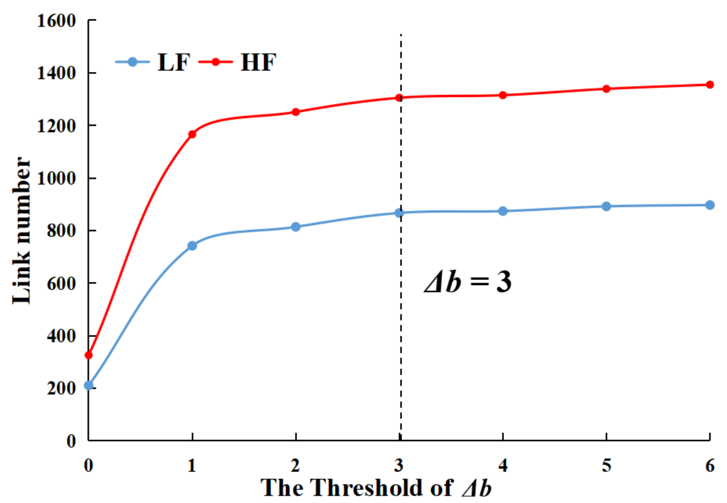

Fig. 7. Sensitivity analysis of the threshold of Δb, showing the number of links plotted against the threshold of Δb during low flow and high flow periods.

4.2 River network topology

The river network topologies of the Yangtze and Indus were constructed after parameter (σ and the threshold of Δb) settings in RivMACNet. Fig. 8 illustrates the connectivity matrix **A** of the study reach, as well as a series of geometrical measures vectorized for visualization including the channel width matrix **B** = $\{b_{i,j}\}$, length matrix **L** = $\{l^{c}_{i,j}\}$ and sinuosity matrix **S** = $\{s_{i,j}\}$. In matrix **A**, nodes within both two networks exhibit strong linear distributions and tend to connect to their neighbours in geographical space because multichannel networks can be described as 'slender' networks (Marra et al., 2014) with limited lateral extension in space, and their lengths are much larger than the multichannel widths. RivMACNet produced fewer nodes n and links m in the Yangtze network (n_1 = 281, m_1 = 339) than in the Indus network during the high flow ($n_{2,HF}$ = 1205, $m_{2,HF}$ = 1339) and low flow ($n_{2,LF}$ = 826, $m_{2,LF}$ = 892) periods, which is related to the reach length and the river pattern (Van den Berg, 1995; Xu, 2004). Additionally, to further compare the differences in links of the Indus between the low and high flow periods, statistics describing the geometrical properties of individual channels in the Indus network are shown in Fig. 9. On average, individual channel lengths during high flow periods are smaller than during low flow periods ($\overline{l_{2,HF}} < \overline{l_{2,LF}}$). This result can be explained by space-filling considerations: the development of a new channel emanating from a node in a space-filling network inevitably intersect neighboring channels and consequently decrease individual channel lengths (Meshkova and Carling, 2014). Although river channels would expand during high flow periods (for example, the number of individual channels with width larger than 1000 m increases in Fig. 9C), an opposite result is observed for the mean widths of the individual channels ($\overline{b_{2,HF}} < \overline{b_{2,LF}}$) because more narrow ($b_{2,HF}$ < 250 m) channels were generated during high flow periods. For the sinuosity, the number of channels where $s_{2,HF}$ > 1.2 decreased significantly during high flow periods, and more straight channels ($s_{2,HF}$ < 1.05) appeared. Nonetheless, the mean values of sinuosity during the high and low flow periods are still close to each other (Fig. 9B). In this context, the increase in the scale (the numbers of nodes and links) of network topology ($n_{2,HF} > n_{2,LF}$, $m_{2,HF} > m_{2,LF}$) implies that the Indus network exhibits more complex planviews during high flow periods, and most of these new individual channels during high flow periods tend to be short, narrow, and straight.

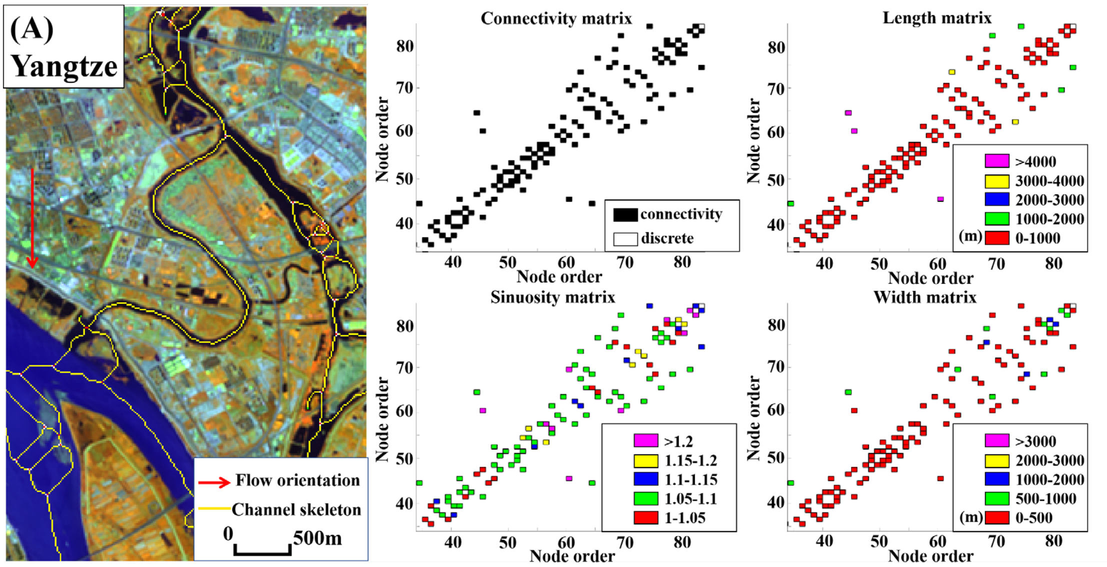

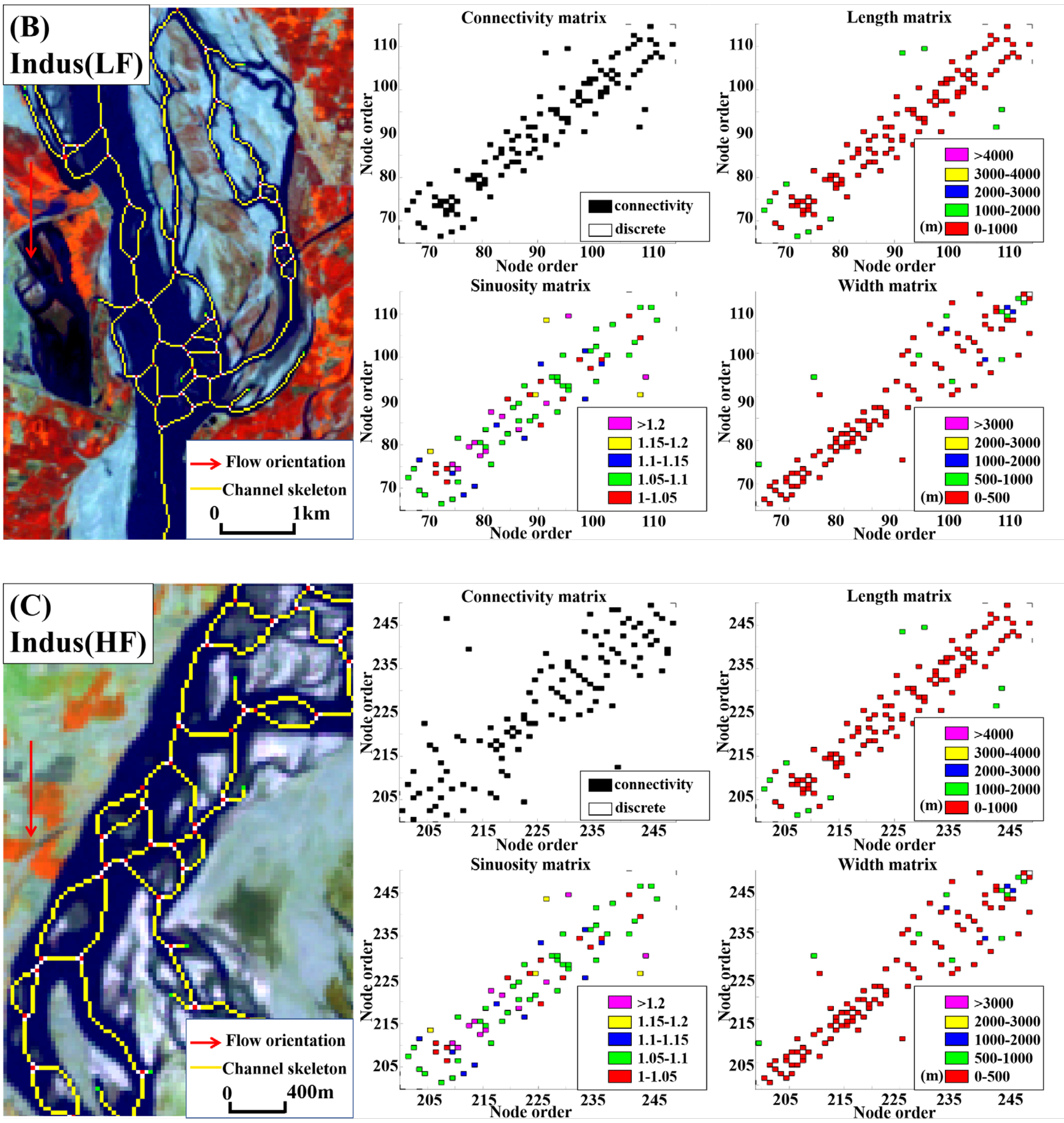

Fig. 8. (Right) An illustrative set of topological and geometrical matrices extracted from (A) the Yangtze network, and the Indus network during (B) LF periods and (C) HF periods. (Left) the water bodies are planviews of the sub-reaches shown by these matrices. For interpretation of the colours in the right matrices see the individual legends. A 50 – node matrix is used to provide the best visual impression of the different colors in each matrix.

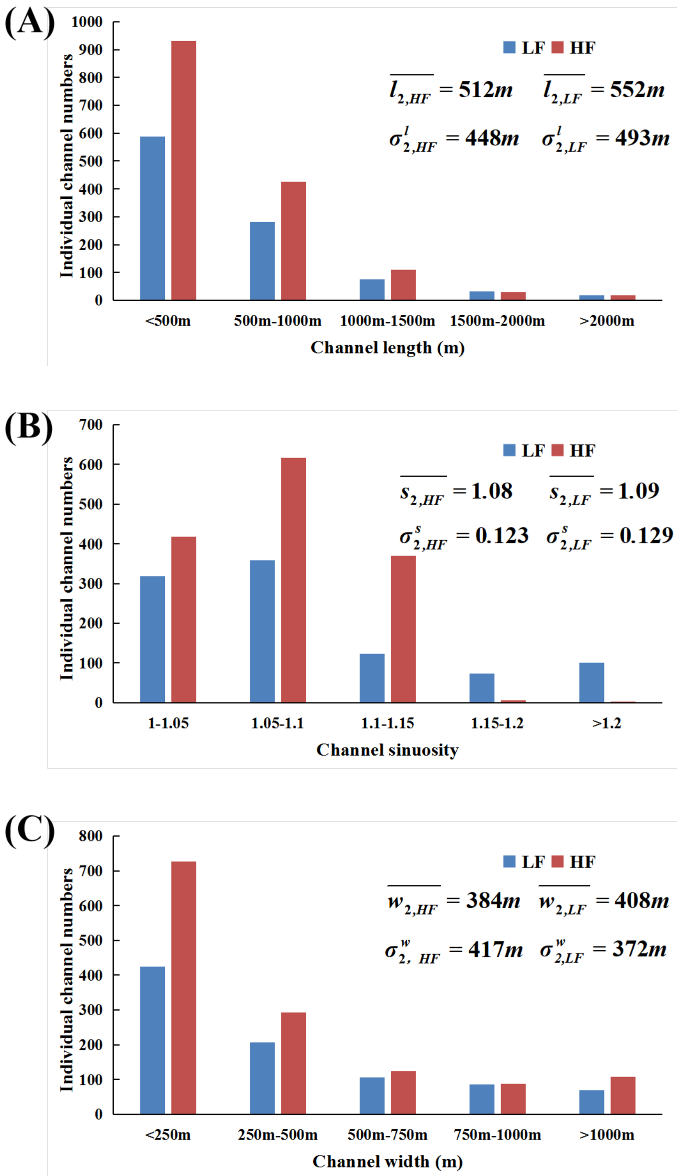

Fig. 9. Distributions of the geometrical properties (A) length, (B) sinuosity and (C) width of the individual channels in the Indus network during high and low flow periods.

4.3 Multichannel network topological measures

Three global topological measures including the weighted degree (WD), clustering coefficient (CC) and the weighted characteristic path length (WCPL) of the two study areas are reported in Table 2. Values of these three weighted topological measures are different between two different river networks, but close when comparing different flow conditions in the same study area. For example, the WD value of the Yangtze network considering the length/width ratio of individual channels as connection strengths is 1.601, smaller than that of the Indus network during LF and HF periods ($\overline{k^{w}_{2,HF}} \approx \overline{k^{w}_{2,LF}} \approx 2.7$). Furthermore, the cumulative distribution of weighted degree P_k, representing the probability that one node has WD value greater than or equal to k, was calculated and plotted in Fig. 10A. The distributions in both Yangtze and Indus networks follow the power-law ($P_k \propto k^{-\lambda}$) distribution and nodes with low weighted degree values ($k_i^w < \overline{k^w}$) account for the largest proportion (70.2% for Yangtze network, and 68.8% and 68.7% for Indus network during HF and LF periods, respectively), followed by a positively skewed long tail (Fig. 10A).

Table 2. Topological measures of the Yangtze and Indus networks at the whole reach scale.

Network	Date	WD	CC	WCPL
Yangtze	April 2019	1.601	0.043	31.516
Indus	March 2011 (LF)	2.667	0.039	71.313
	October 2011 (HF)	2.689	0.026	75.722

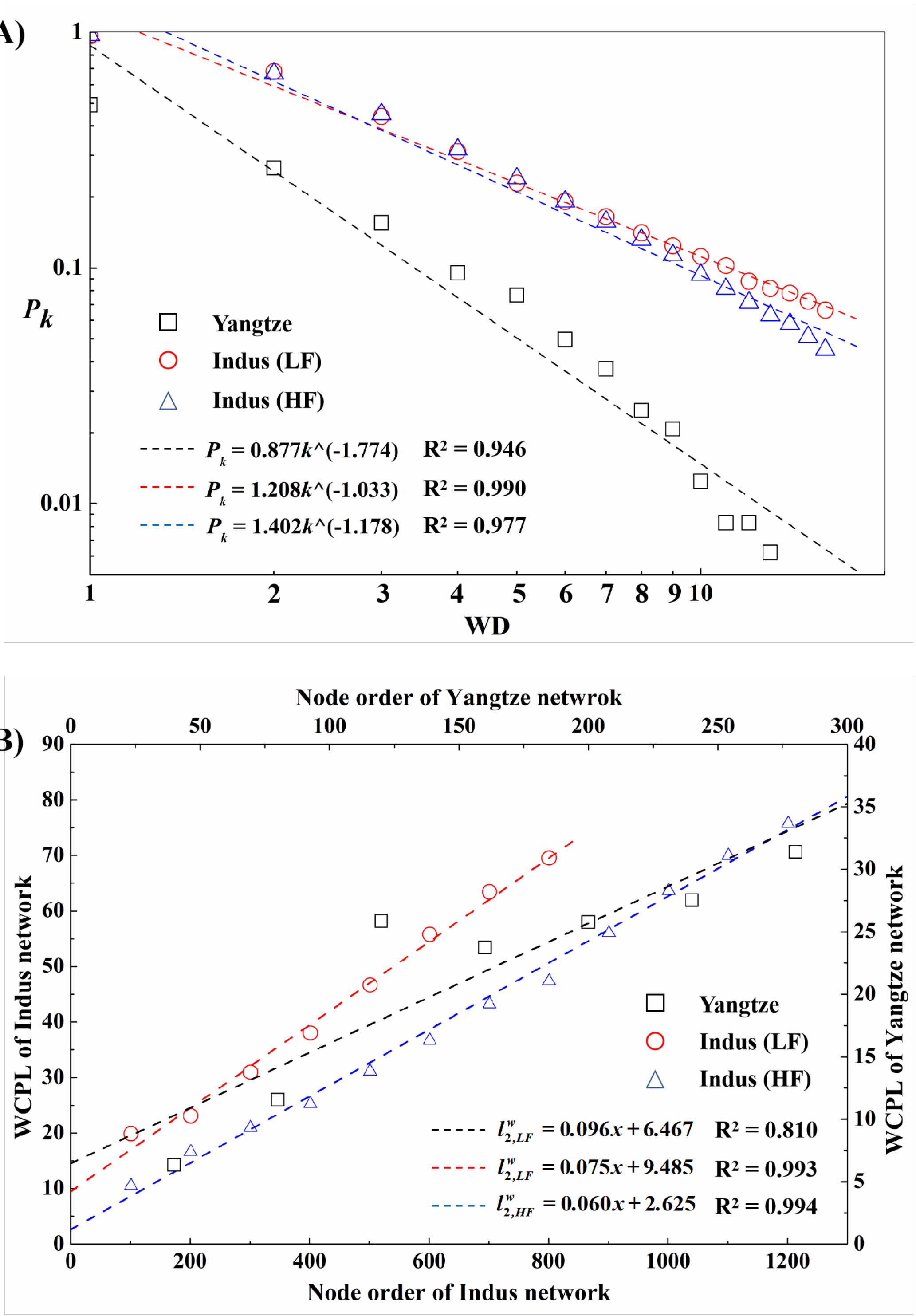

Fig. 10. (A) The cumulative distributions of weighted degree (WD) of the Yangtze and Indus networks during high and low flow periods. (B) The relationship between the weighted characteristic path length (WCPL) and node number for the Yangtze and Indus networks. The step size of the node numbers *Δn* are 40, and 100 for Yangtze and Indus, respectively.

In contrast to the maximum clustering coefficient (CC) value of 1, global CC values for both Yangtze and Indus networks are small, implying that these two river networks have a poor transitivity (Newman, 2003). This outcome may be due to the existence of a considerable number of end nodes caused by 'blind spurs' with a CC value of 0 (Fig. 11). Moreover, the clustering coefficient assesses only the density of 'triangle patterns' defining sand bars and islands, but ignores higher order structures like 'quadrilaterals' in multichannel networks (Fig. 11). Due to limited computational resources, we considered only CC values of quadrilaterals (cycles of length 4), $C_i^4 = \frac{\sum_{j,h,k \in n} a_{ij}a_{jh}a_{hk}a_{ki}}{k_{i,nn}k_i(k_i\text{-}1)}$, based on the extendibility of the expression in Table 1 (Caldarelli et al., 2004). As a result, similar to the third-order CC, fourth order CC values of both Yangtze and Indus networks were also small; 0.006 for the former, while 0.015 and 0,012 for the latter during LF and HF periods.

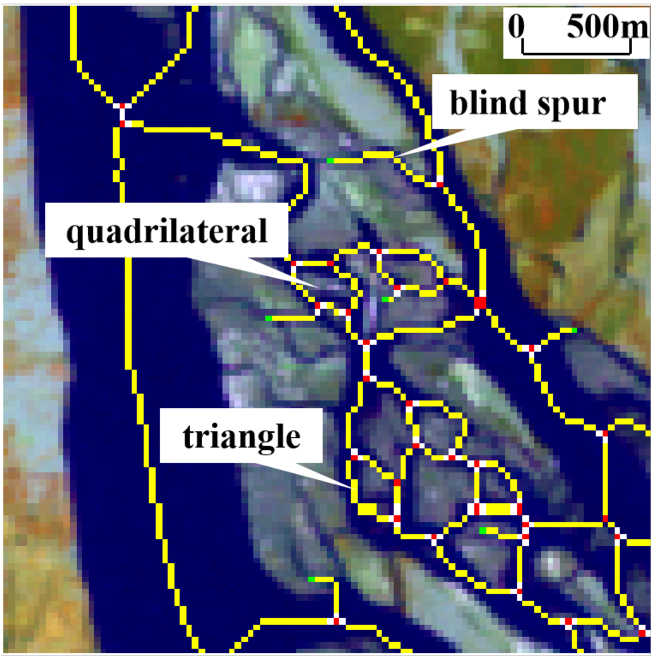

Fig. 11. Illustration of blind spurs, triangles, and quadrilaterals located in the multichannel network.

The weighted characteristic path length (WCPL) serves as a measurement of the mean shortest water and sediment transport distance between pairs of bifurcation nodes within a river network. In order to explore the relationship between the WCPL value and the node numbers within river networks, an ordered subset of the nodes was used to create the sub-networks. The ordered subset starts from the most upstream node of the multichannel network, and the number of nodes in the subset increases gradually by a given step size *Δn.* The corresponding WCPL value of each sub-network of the Yangtze and Indus networks was calculated (Fig. 10B). The results indicate that WCPL remarkably scales linearly with the network scale in any study area ($l^w \propto m$), although values of WCPL varies greatly between two river networks (Table 2). Additionally, as shown in Fig. 10B, the WCPL of the Indus network during high flow periods is smaller than that during low flow periods with the same number of nodes due to the larger proportion of short channels during high flow periods (Fig. 9A).

4.4 Spatial evolution of topological measures at a sub-network scale

RivMACNet also examined the spatial evolution of the multichannel network (i.e., Indus network in this study) topology. The radius of the circular moving window R for assessment of local topological properties was set to 3 km, slightly larger than the multichannel width of the Indus network to prevent nodes from being ignored. Fig. 12 illustrates the spatial evolution of topological measures at the subnetwork scale (R = 3 km) along the multichannel centerline of the Indus during both high and low periods. In contrast to the global measures, three local measures vary along the Indus network, indicating that the Indus network topology is irregular. Furthermore, the trends in Fig. 12 are likely to be the sum of a series of sine functions of varying periods and amplitudes, rather than monotonic. Thus, a continuous wavelet transform (CWT) was used to analyze the dominant periods T_a in the spatial evolution of the Indus network topology. For brevity this method is not explained here, but is reported in detail by Kharitonenko et al. (2002) and Liang et al. (2010). The wavelet coefficients *W_f (a, b)* and their variance values *Var (a)* of the three topological measures are illustrated in Fig. 13, which shows that the aforementioned topological measures exhibit similar spatial evolution periods under the same flow conditions. Although no clear long-distance trends were observed, 8 - to - 12 km periods during high flow, and 15 - to - 37 km periods during low flow are identified shown by the white horizontal lines, implying that the Indus network exhibits beaded planforms such that, multiple channel reaches are interspersed with reaches with fewer channels.

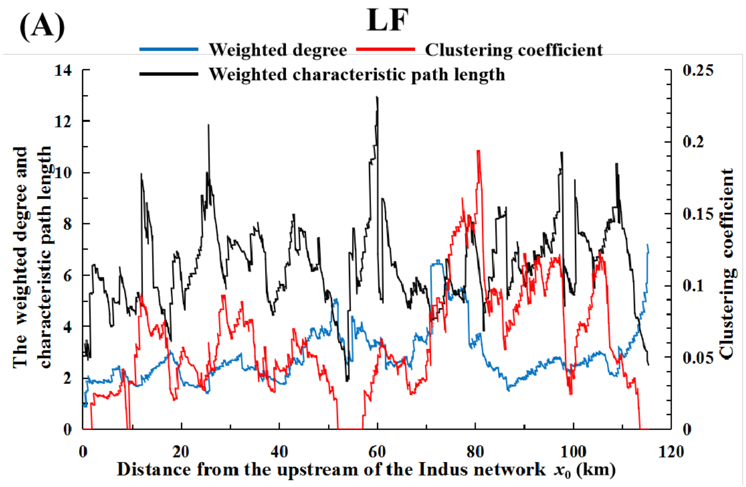

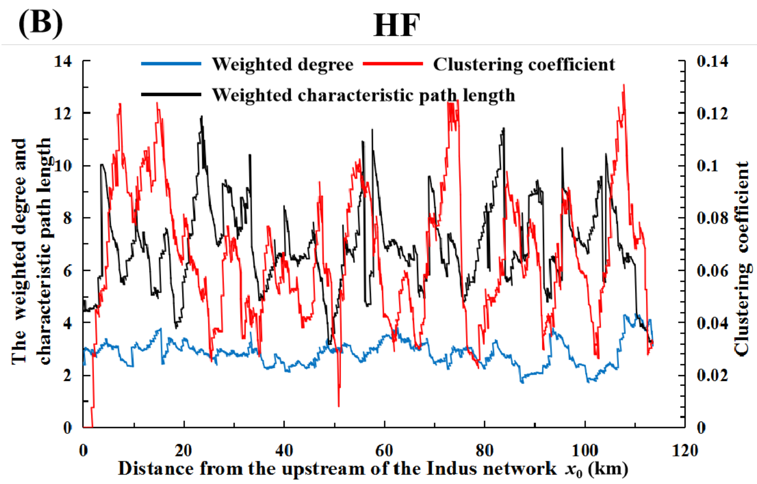

Fig. 12. Spatial distributions of three topological measures, including weighted degree, cluster coefficient and the weighted characteristic path length, at the subnetwork scale (*R*

= 3 km) along the multichannel centerline of the Indus network during (A) low and (B) high flow periods.

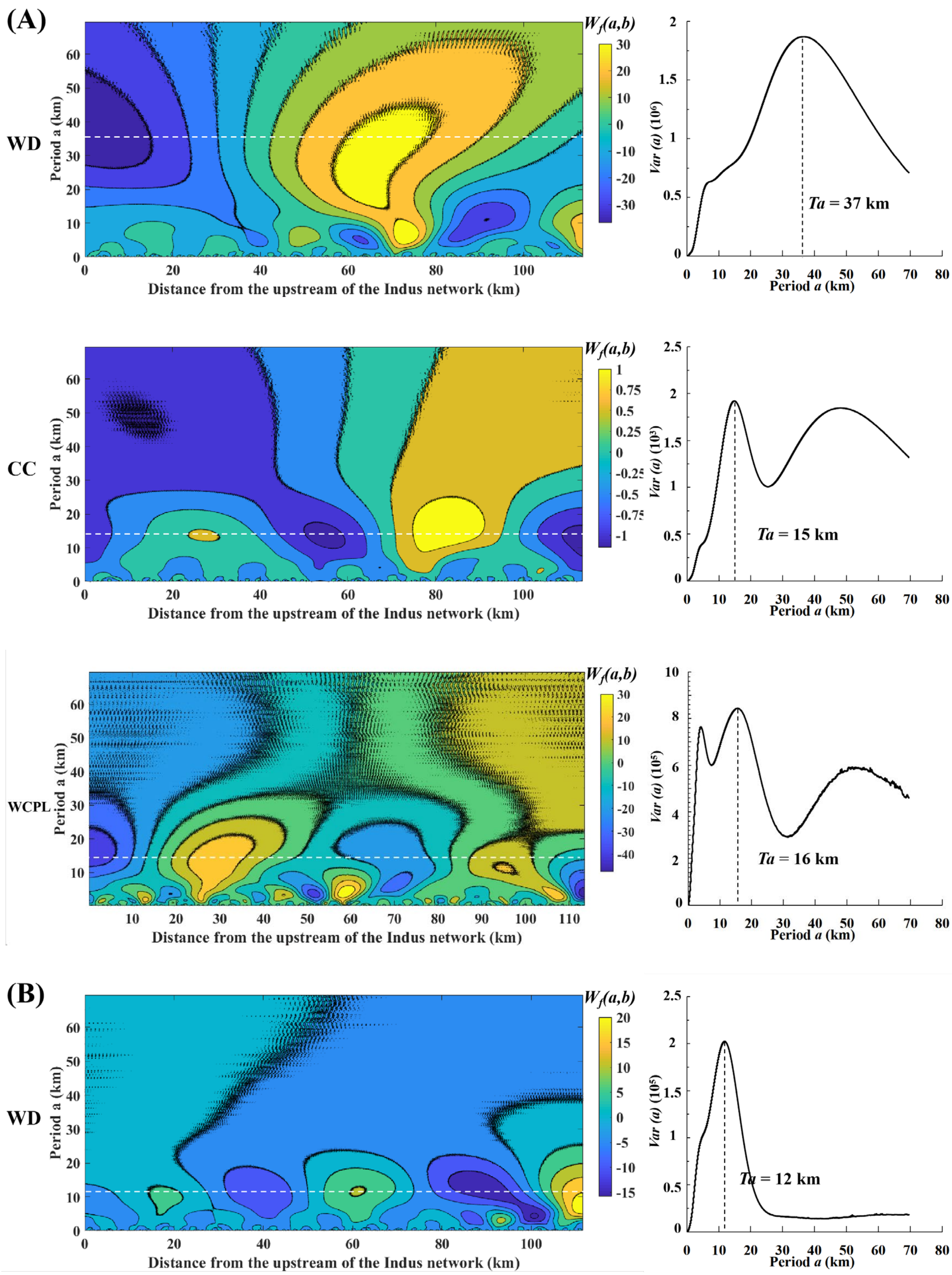

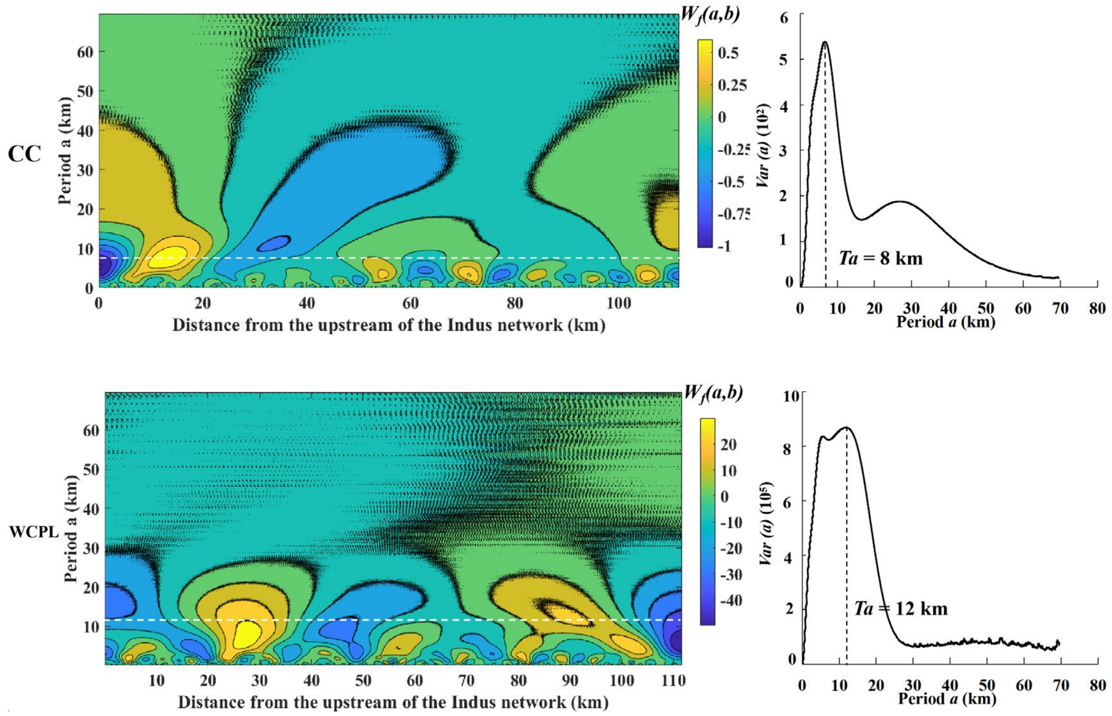

Fig. 13. (Left) Contours of the wavelet coefficient $W_f\,(a, b)$ and (Right) its variance values *Var (a)* against the period of the local topological measures: weighted degree (WD), clustering coefficient (CC) and weighted characteristic path length (WCPL) in the Indus network during (A) low and (B) high flow periods. The dominant periods T_a in the spatial evolution can be reflected by the maximum values of *Var (a)*, and marked by white horizontal lines in the contours of $W_f\,(a, b)$.

5. Discussion

5.1 Reliability of RivMACNet

To assess the reliability and performance of RivMACNet, another popular river analysis engine RivaMap (Isikdogan et al., 2017) was applied to the Yangtze network and the Indus network during high flow periods (see http://live.ece.utexas.edu/research/rivamap/). The three following issues were considered when comparing these two methods:

1) Computation complexity. We executed the RivMACNet and RivaMap on MATLAB R2016a using a PC (CPU: Intel Core i5-4590T at 2 GHz, RAM: 8 GB, Windows10). It took 595s and 1527s for RivaMap to construct the topologies of the Yangtze and Indus networks. This time period is longer than for RivMACNet

which took 254s and 629s, respectively. The difference between the two methods suggests that RivMACNet has a significantly higher computational efficiency and because the total time consumed will increase with the scale of river network, this difference is likely to be larger in practice.

2) Comparison of network topological measures. 281 nodes and 339 links were detected in the Yangtze network in RivMACNet, larger than numbers (less than 220 nodes and 240 links in the same study area) reported by Chen et al. (2019). These differences are caused by the MNDWI threshold and node detection method. Additionally, the constructed maps of the study reaches were derived using the line with length $b_{i,j}^{k}$ (expression (8)) orthogonal to the channel local orientation $slop_{i,j}^{k}$ (expression (6)) at each skeleton pixel (or centerline point in RivaMap) in RivMACNet. These constructed maps are shown in Fig. 14 with ground reference data on water bodies presented as background. Given the ground-reference images, we calculated and compared the precision and recall of the channel images constructed by the two methods (Table 3):

$$Precision = \frac{TP}{TP+FP}; \tag{10}$$

$$Recall = \frac{TP}{TP+FN}; \tag{11}$$

where *TP* indicates the number of pixels considered as water bodies in both ground - reference images and RivMACNet (or RivaMap), while *FP*(*FN*) indicate the number of pixels considered as water bodies (non-water bodies) in ground - reference images, but non-water bodies (water bodies) in RivMACNet or RivaMap. For the Yangtze network, the precision values for RivMACNet and RivaMap are close, and the main false positives refer to isolated channels caused by the small *MNDWI* (red pixels in I shown in Fig. 14). However, RivaMap produced a low precision in the constructed map of the Indus, missing large slices of channels (pink pixels in II shown in Fig. 14). This lack of precision is because RivaMap is unable to guarantee the connectivity of the constructed channels, especially for multichannel networks with a large number of bifurcations (Isikdogan et al, 2017). An individual channel may be cut into several short and discontinuous channels, of which some small connected areas were mistakenly regarded as noise and then omitted when regenerating river channels. Additionally, values of recall of RivMACNet are slightly larger than that of RivaMap, indicating that RivMACNet is more sensitive to the presence of small islands and sand bars (green pixels in III shown in Fig. 14), which play important roles in the multichannel network study.

Table 3. Precision and recall of RivMACNet and RivaMap.

	Precision (%)		*Recall* (%)	
	Yangtze	Indus	Yangtze	Indus
RivMACNet	98	95	91	91
RivaMap	92	71	88	87

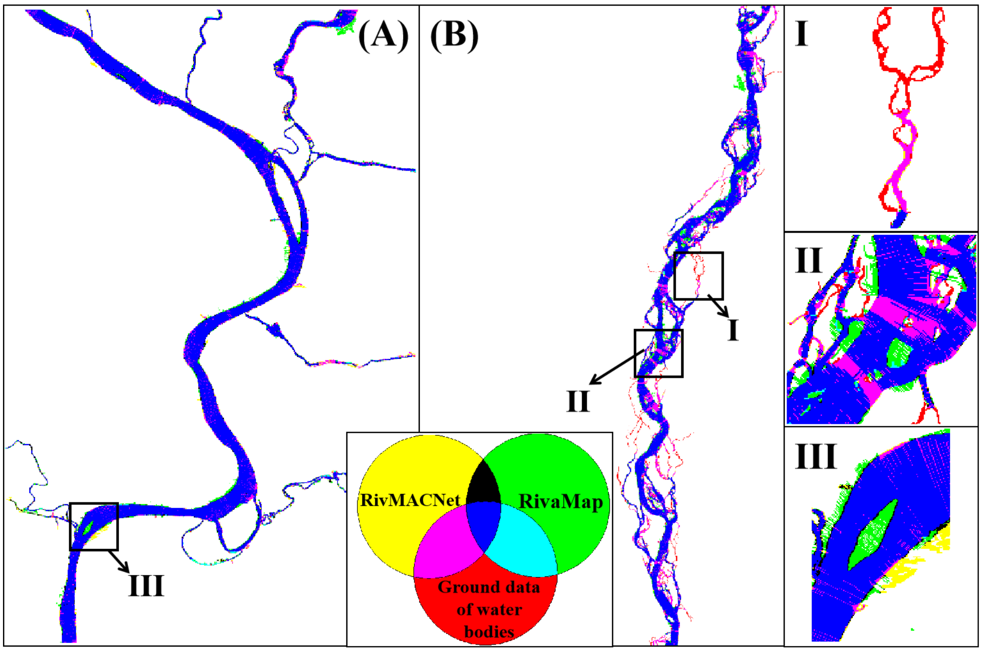

Fig. 14. Comparison between the constructed (A) Yangtze and (B) Indus maps produced using RivMACNet and RivaMap using ground reference data on water bodies as background. (I), (II), and (III) are zoomed images of (A) and (B), respectively. Sporadic water bodies in size *Area* (*Area* $< 0.05 \times M \times N$ in this paper) are considered as noise, and have been omitted in RivaMap constructed maps and the ground data.

3) Comparison of network planview measures. Clearly, the ability of RivaMap to derive reliable individual channel lengths and sinuosity, as well as node and link counts is limited by its poor performance in maintaining river connectivity. In this context, we considered the individual channel widths and compared these between RivaMap and RivMACNet because the extraction process is almost unaffected by network connectivity. In contrast to the centerlines of individual channels in RivaMap, the channel skeleton is applied for channel width extraction in RivMACNet. Thus, we computed the average of the width estimates for the centerline points in RivaMap that were within a given distance (herein referred to as one resolution unit) from the skeletons to ensure the same individual channels in RivMACNet were compared. In this manner, we examined 254 and 1141 individual channels of the Yangtze and Indus network, respectively, and then calculated the Spearman correlation coefficient (Spearman, 1987) of individual channel widths produced by RivMACNet and RivaMap. A significant correlation (Spearman correlation coefficients of 0.988 and 0.915 for the Yangtze and Indus networks, respectively) between the two channel width datasets produced by RivMACNet and RivaMap was observed (Fig. 15), implying that river network measures (*e.g.*, individual channel width) extracted by RivMACNet are similar to those produced by RivaMap.

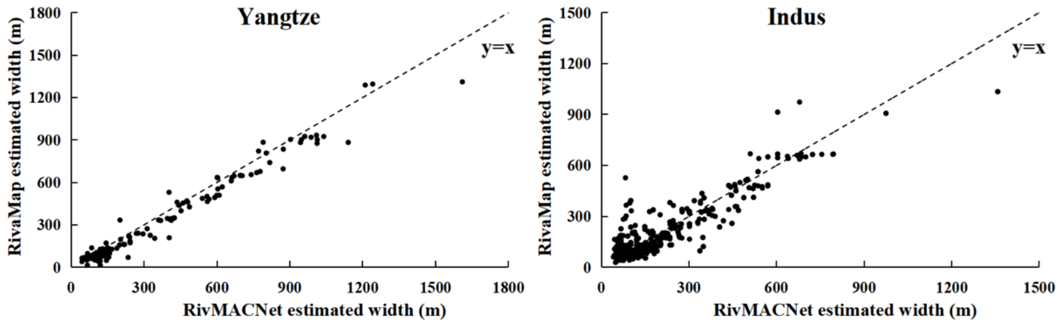

Fig. 15. Comparison of the estimates of river width produced by RivMACNet and RivaMap.

5.2 Limitations

Although RivMACNet has been demonstrated to be superior in guaranteeing the connectivity of multichannel networks, the RivMACNet results remain limited by the quality of the input data and methods used. First, user decisions are a central component of RivMACNet and include selecting parameters such as a set of thresholds for *MNDWI*, the noise removal window size σ, width gate Δb, and sub-network radius R. Although these decisions could be made based on prior knowledge, any uncertainty associated with these parameter values could be transferred to the outputs. Second, RivMACNet poorly detects individual channels with width close to or less than the spatial resolution of the input images. The same limitation also apply to other routines such as RivaMap. Third, in contrast to field surveys, errors and uncertainty associated with geospatial data also are important issues that need to be considered in the river network analysis (Downward et al., 1994). The likely sources of errors and uncertainty in RivMACNet can be summarised as follows: (i) errors caused by transforming the longitude and latitude of the river network in the real-world to the corresponding *X* and *Y* pixel coordinates in the digital maps; (ii) uncertainty caused by delineating the boundaries of river channel extent in digitized maps (Leonard et al., 2020); (iii) errors due to the definition of the river network as a directed and weighted network, with the directions of its links determined simply by the distances from nodes connected to them to the upstream of the multichannel network. A 3D representation achieved using a digital elevation model (DEM) could increase accuracy, especially for lateral individual channels in river networks.

6. Conclusions

We presented a new automatic multichannel network analysis method called RivMACNet for: (i) constructing multichannel network topology; (ii) calculating geometrical measures including individual channel lengths, widths and sinuosities and (iii) calculating topological measures including the weighted degree (WD), clustering coefficient (CC) and weighted characteristic path length (WCPL) at the reach and subnetwork scales. The method used, as input, satellite sensor images of *MNDWI*, although other variable inputs are possible. We tested RivMACNet on the meandering reach of the Yangtze River near Wuhan, and the braided reach of the Indus River, Pakistan, and analyzed their topological properties at different scales.

Comparison between RivMACNet and other alternative conventional methods demonstrated that RivMACNet is a reliable tool for assessing and analyzing multichannel topology because: (i) RivMACNet is more sensitive to islands and sand bars located in multichannel rivers; (ii) RivMACNet has a higher computational efficiency and precision and (iii) RivMACNet can maintain network connectivity.

Network analysis of reaches of the Yangtze and Indus Rivers indicated that multichannel networks exhibited a strong linear, but beaded (Meshkova and Carling, 2013) planview such that reaches with multiple parallel channels are interspersed with reaches with fewer, or only one channel. The topological measures (*e.g.*, WD, CC and WCPL in this study) at the reach scale were found to be independent of discharge. The small CC values imply poor transitivity in both Yangtze and Indus networks. Additionally, the dominant topological scale of the Indus network varied periodically along the river reach (8 - to-12 km for HF periods, and 15 – to - 37 km for LF periods).

The proposed RivMACNet method has considerable application prospect for the analysis of complex river networks, providing a new lens through which to analyze river network behaviour. In the future, research should focus on other multichannel networks using time-series datasets and compare the similarities and differences between topological measures characterizing these multichannel networks in nature, with the general aim to discover the physical bases of river networks.

Authorship statement

LYH developed the conception and design of study, wrote the necessary scripts, performed analysis, and wrote the manuscript. PMA helped in the conception and design of study, guided the methodological analysis, helped write the manuscript, and revised the manuscript critically for important intellectual content. PAC originated the conception and design of study, guided the analysis, helped write the manuscript, and revised the manuscript critically for important intellectual content. WYJ acquired the data, and participated in the analysis. JEH acquired the data, and participated in the analysis.

Declaration of competing interest

The authors declare that they have no known competing financial interests or personal relationships that could have appeared to influence the work reported in this paper.

Computer code availability

RivMACNet are available at http://github.com/lyh444/RivMACN.git. The code developer was Yanhui Liu (Address: Hohai University, Nanjing, China. Contact number: + 86 - 15850553774. E-mail address: liuyanhui@hhu.edu.cn.) RivMACNet is implemented and tested in MATLAB R2016a. Everyone is granted permission to copy, modify and redistribute this code, but under the condition that the original algorithm copyright is preserved.

Acknowledgements

This research was funded and supported partially by the National Key Research and Development Program of China (No. 2021YFC3200400), the National Natural Science Foundation of China (NSFC, No. 42041004), the Provincial Science Fund for Excellent Young Scholars of Henan (No. 202300410540), the China Scholarship Council (No. CSC201906710092) and Hohai University, Nanjing. The research was undertaken while Liu Yanhui visited Lancaster University in 2020.

References

Ali A., 2013. Indus basin floods: Mechanisms, impacts, and management. Asian Development Bank, Mandaluyong City, Philippines.

Ashour, M. A., Saad, M. S., Kotb M. M., 2017. Evaluation of alluvial channels meandering phenomenon (case study Bahr Youssef). Annals of Valahia University of Targoviste, Geographical Series, 17(2): 206 – 219.

Bai R., Tiejian L., Huang Y., et al., 2015. A hierarchical pyramid method for managing large-scale high-resolution drainage networks extracted from DEM. Computers & Geosciences 85: 234-247. https://doi.org/10.1016/j.cageo.2015.06.019

Bridge J. S., 2009. Rivers and floodplains: forms, processes, and sedimentary record. John Wiley & Sons.

Caldarelli G., Pastor-Satorras R., Vespignani A., 2004. Structure of cycles and local ordering in complex networks. The European Physical Journal B, 38(2): 183-186. https://doi.org/10.1140/epjb/e2004-00020-6

Carling P. A., Jansen J., Meshkova L., 2014. Multichannel rivers: their definition and classification. Earth Surface Processes and Landforms, 39(1): 26-37. https://doi.org/10.1002/esp.3419

Carling P. A., Trieu H., Hornby D. D., et al., 2018. Are equilibrium multichannel networks predictable? The case of the regulated Indus River, Pakistan. Geomorphology 302: 20-34. https://doi.org/10.1016/j.geomorph.2017.09.021

Chen W., Sui L., Xu Z., et al., 2012. Improved Zhang-Suen thinning algorithm in binary line drawing applications//International Conference on Systems and Informatics (ICSAI2012). IEEE: 1947-1950. https://doi.org/10.1109/ICSAI.2012.6223430

Chen X., Shen X., Li H., et al., 2019. Construct Channel Network Topology From Remote Sensing Images by Morphology and Graph Analysis. IEEE Geoscience and Remote Sensing Letters. http://10.1109/LGRS.2019.2942107

Chew L. C., Ashmore P. E., 2001. Channel adjustment and a test of rational regime theory in a proglacial braided stream. Geomorphology, 37(1-2): 43-63. https://doi.org/10.1515/avutgs- 2017-0019

Dodds P. S., Rothman D. H., 2000. Geometry of river networks. I. Scaling, fluctuations, and deviations. Physical Review E, 63(1): 016115. https://doi.org/10.1103/PhysRevE.63.016115

Downward S. R., Gurnell A. M., Brookes A., 1994. A methodology for quantifying river channel planform change using GIS. IAHS Publications-Series of Proceedings and Reports-Intern Assoc Hydrological Sciences, 224: 449-456.

Environment and GIS Support Project for Water Sector Planning (EGIS), 2002. Developing and updating Empirical Methods for Predicting Morphological Changes of Jamuna River Information System. EGIS Technical Note Series 29, Dhaka, Bangladesh.

Floyd R. W., 1962. Algorithm 97: shortest path. Communications of the ACM, 5(6): 345. https://doi.org/10.1145/367766.368168

Grabowski R. C., Surian N., Gurnell A. M., 2014. Characterizing geomorphological change to support sustainable river restoration and management. Wiley Interdisciplinary Reviews: Water 1(5): 483-512. https://doi.org/10.1002/wat2.1037

Guo Q., Pu R., Li J., et al., 2017. A weighted normalized difference water index for water extraction using Landsat imagery. International Journal of Remote Sensing 38(19): 5430-5445. https://doi.org/10.1080/01431161.2017.1341667

Gupta A., 2008. Large Rivers: Geomorphology and Management. John Wiley and Sons: Chichester.

Gupta N., Atkinson P. M., Carling P. A., 2013. Decadal length changes in the fluvial planform of the River Ganga: bringing a mega-river to life with Landsat archives. Remote Sensing Letters, 4(1): 1-9. https://doi.org/10.1080/2150704X.2012.682658

Hiatt M., Sonke W., Addink E. A., et al., 2020. Geometry and topology of estuary and braided river channel networks automatically extracted from topographic data. Journal of Geophysical Research: Earth Surface, 2020, 125(1): e2019JF005206. https://doi.org/10.1029/2019JF005206

Harrison L. R., Legleiter C. J., Wydzga M. A., et al., 2011. Channel dynamics and habitat development in a meandering, gravel bed river. Water Resources Research, 47(4). https:// doi. org /10.1029/2009WR008926

Hasthorpe J., Mount N., 2007. The generation of river channel skeletons from binary images using raster thinning algorithms. Proceedings of The Geographical Information Science Research UK Conference. Maynooth, Ireland: 477-483.

Howard A. D., Keetch M. E., Vincent C. L., 1970. Topological and geometrical properties of braided streams. Water Resources Research, 6(6): 1674-1688. https://doi.org/10.1029/WR006i006p01674

Inam A., Clift P. D., Giosan L., et al., 207. The geographic, geological and oceanographic setting of the Indus River. Large rivers: geomorphology and management, 2007: 333-345.

Isikdogan F., Bovik A., Passalacqua P., 2017. RivaMap: An automated river analysis and mapping engine. Remote Sensing of Environment 202: 88-97. https://doi.org/10.1016/j.rse.2017.0 3.044

Jansen J. D., Nanson G. C., 2010. Functional relationships between vegetation, channel morphology, and flow efficiency in an alluvial (anabranching) river. Journal of

Geophysical Research: Earth Surface, 2010, 115(F4). http://dx.doi.org/10.1029/2010JF001657

Kale V. S., 2014. Is flooding in South Asia getting worse and more frequent?. Singapore Journal of Tropical Geography, 35(2): 161-178. https://doi.org/10.1111/sjtg.12060

Kharitonenko I., Zhang X., Twelves S., 2002. A wavelet transform with point – symmetric extension at tile boundaries. IEEE Transaction on Image Processing, 11(12): 1357 – 1364. http://dx.doi.org/10.1109/TIP.2002.806237

Kleinhans M. G., Ferguson R. I., Lane S. N., et al., 2013. Splitting rivers at their seams: bifurcations and avulsion. Earth Surface Processes and Landforms, 38(1): 47-61. https://doi.org/10.1002/esp.3268

Kleinhans M., van Kreveld M., Ophelders T., et al., 2019. Computing representative networks for braided rivers. Journal of Computational Geometry, 10(1): 423–443-423–443. https://doi.org/10.20382/jocg.v10i1a14

Leonard C. M., Legleiter C. J., Lea D. M., et al., 2020. Measuring channel planform change from image time series: A generalizable, spatially distributed, probabilistic method for quantifying uncertainty. Earth Surface Processes and Landforms, 45(11): 2727-2744. https://doi.org/10.1002/esp.4926

Leopold L. B., Wolman M. G., 1957. River channel patterns: braided, meandering, and straight. US Government Printing Office.

Li J., Xia J., Zhou M., et al., 2017. Variation in reach-scale thalweg-migration intensity in a braided reach of the lower Yellow River in 1986–2015. Earth Surface Processes and Landforms, 42(13): 1952-1962. https://doi.org/10.1002/esp.4154

Liang S., Ge S., Wan L., et al., 2010. Can climate change cause the Yellow River to dry up? Water Resources Research, 46(2). https://doi.org/10.1029/2009WR007971

Liu Y., Wang Y., Jiang E., 2021. Stability index for the plainview morphology of alluvial rivers and a case study of the Lower Yellow River. Geomorphology, 389: 107853. https://doi.org/10.1016/j.geomorph.2021.107853

Marra W. A., Kleinhans M. G., Addink E. A., 2014. Network concepts to describe channel importance and change in multichannel systems: test results for the Jamuna River, Bangladesh. Earth Surface Processes and Landforms, 39(6): 766-778. https://doi.org/10.1002/esp.3482

McFeeters S. K., 1996. The use of the Normalized Difference Water Index (NDWI) in the delineation of open water features. International Journal of Remote Sensing, 17(7): 1425-1432. https://doi.org/10.1080/01431169608948714.

Meshkova L. V., Carling P. A., 2013. Discrimination of alluvial and mixed bedrock–alluvial multichannel river networks. Earth Surface Processes and Landforms, 38(11): 1299-1316. https://doi.org/10.1002/esp.3417

Miller T. K., 1988. Stream channel pattern: A threshold model. Physical Geography, 9(4): 373-384. https://doi.org/10.1080/02723646.1988.10642361

Monegaglia F., Zolezzi G., Güneralp I., et al., 2018. Automated extraction of meandering river morphodynamics from multitemporal remotely sensed data. Environmental Modelling & Software 105: 171-186. https://doi.org/10.1016/j.envsoft.2018.03.028.

Mount N. J., Louis J., Teeuw R. M., et al., 2003. Estimation of error in bankfull width comparisons from temporally sequenced raw and corrected aerial photographs. Geomorphology, 56 (1-2): 65-77. https://doi.org/10.1016/S0169-555X(03)00046-1

Nanson G. C., Knighton A. D., 1996. Anabranching rivers: their cause, character and classification. Earth Surface Processes and Landforms, 21(3): 217-239. https://doi.org/10.1002/(SICI)1096-9837(199603)21:3<217::AID-ESP611>3.0.CO;2-U

Newman M. E. J., 2003. The structure and function of complex networks. SIAM Review 45(2): 167-256. https://doi.org/10.1137/S003614450342480

Oliver S., 2008. Image Analysis, Classification and Change Detection in Remote Sensing (With Algorithms for ENVI/IDL). Computers & Geosciences, 34(1). https://doi.org/10.1137/S003614450342480

Olsen M. A., Hartung D., Busch C., et al., 2011. Convolution approach for feature detection in topological skeletons obtained from vascular patterns//2011 IEEE Workshop on Computational Intelligence in Biometrics and Identity Management (CIBIM). IEEE:

163-167. https://doi.org/10.1109/CIBIM.2011.5949223.
Osman A. M., Thorne C. R., 1998. Riverbank stability analysis. I: Theory. Journal of Hydraulic Engineering, 114(2): 134-150. https://doi.org/10.1061/(ASCE)0733-9429(1988)114:2(134)
Parker G., Anderson A. G., 1975. MODELING OF MEANDERING AND BRANDING IN RIVERS[C]//PROC. 2ND ANNUAL SYMP. OF WATERWAYS, HARBOURS AND COASTAL ENGNG. DIV. ASCE ON MODELING TECHNIQUES, (MODELING'75: SAN FRANCI., 1(SEPTEMBER 3-5, 1975)): 575-591.
Parker G., 1976. On the cause and characteristic scales of meandering and braiding in rivers. Journal of Fluid Mechanics, 76(3): 457-480. https://doi.org/10.1017/S0022112076000748
Parker G., Shimizu Y., Wilkerson G. V., et al., 2011. A new framework for modeling the migration of meandering rivers. Earth Surface Processes and Landforms, 36(1): 70-86. https://doi.org/10.1002/esp.2113
Pavelsky T. M., Smith L. C., 2008. RivWidth: A software tool for the calculation of river widths from remotely sensed imagery. IEEE Geoscience and Remote Sensing Letters 5(1): 70-73. https://doi.org/10.1109/LGRS.2007.908305
Petropoulos G. P., Kalaitzidis C., Vadrevu K. P., 2012. Support vector machines and object-based classification for obtaining land-use/cover cartography from Hyperion hyperspectral imagery. Computers & Geosciences , 41: 99-107. https://doi.org/10.1016/j.cageo.2011.08.019
Richardson W. R., 2002. Simplified model for assessing meander bend migration rates. Journal of Hydraulic Engineering 128(12): 1094-1097. https://doi.org/10.1061/(ASCE)0733-9429 (2002)128:12(1094)
Rodríguez-Iturbe I., Rinaldo A., 2001. Fractal river basins: chance and self-organization. Cambridge University Press.
Rubinov M., Sporns O., 2010. Complex network measures of brain connectivity: uses and interpretations. Neuroimage 52(3): 1059-1069. https://doi.org/10.1016/j.neuroimage.20 09.10.003.
Rust B. R., 1978. A classification of alluvial channel systems. In fluvial Sedimentology, Mial AD (ed). Canadian Society of Petroleum Geologist: Calgary, Canada; 187-198.
Schaefer E. I., Pelletier J. D., 2020. An algorithm to reduce a river network or other graph-like polygon to a set of lines. Computers & Geosciences, 145: 104554. https://doi.org/10.1016/j.cageo.2020.104554
Schwenk J., 2016. Meandering rivers: interpreting dynamics from planform geometry and the secret lives of migrating meanders. University of Minnesota. https://doi.org/10.1108/K-02-2018-0092
Schwenk J., Hariharan J., 2021. RivGraph: Automatic extraction and analysis of river and delta channel network topology. Journal of Open Source Software, 2021, 6 (LA-UR-21-20218). https://doi.org/10.21105/joss.02952
Shahrood A. J., Menberu M. W., Darabi H., et al., 2020. RiMARS: An automated river morphodynamics analysis method based on remote sensing multispectral datasets. Science of the Total Environment, 719: 137336. https://doi.org/10.1016/j.scitotenv.2020.137336
Shen X., Hong Y., Zhang K., et al., 2017. Refining a distributed linear reservoir routing method to improve performance of the CREST model. Journal of Hydrologic Engineering, 22(3): 04016061. https://doi.org/10.1061/(ASCE)HE.1943-5584.0001442
Smith M. J., Pain C. F., 2009. Applications of remote sensing in geomorphology. Progress in Physical Geography, 33(4): 568-582. https://doi.org/10.1177/0309133309346648
Spearman C., 1987. The proof and measurement of association between two things. The American Journal of Psychology, 100(3/4): 441-471. https://doi.org/10.2307/1422689
Syvitski J. P. M., Brakenridge G. R., 2013. Causation and avoidance of catastrophic flooding along the Indus River, Pakistan. GsA today, 23(1): 4-10.
Tokunaga E., 1966. The composition of drainage network in Toyohira River Basin and valuation of Horton's first law. Geophys. Bull. Hokkaido Univ., 15: 1-19.

Tooth S., Nanson G. C., 2004. Forms and processes of two highly contrasting rivers in arid central Australia, and the implications for channel-pattern discrimination and prediction. Geological Society of America Bulletin, 116(7-8): 802-816. https://doi.org/10.1130/B25308.1

Van den Berg J. H., 1995. Prediction of alluvial channel pattern of perennial rivers. Geomorphology, 12(4): 259-279. https://doi.org/10.1016/0169-555X(95)00014-V

Van Niekerk A. W., Heritage G. L., Moon B. P., 1995. River classification for management: the geomorphology of the Sabie River in the eastern Transvaal. South African Geographical Journal, 77(2): 68-76.https://doi.org/10.1080/03736245.1995.9713594

Watts D. J., Strogatz S. H., 1998. Collective dynamics of ‘small-world’ networks. Nature, 393(6684): 440-442. https://doi.org/10.1038/30918

Williams P. F., Rust B. R., 1969. The sedimentology of a braided river. Journal of Sedimentary Research, 39(2): 649-679. https://doi.org/10.1306/74D71CF3-2B21-11D7-8648000102C1865D

Xu H., 2006. Modification of normalised difference water index (NDWI) to enhance open water features in remotely sensed imagery. International Journal of Remote Sensing, 27(14): 3025-3033. https://doi.org/10.1080/01431160600589179

Xu J., 2004. Comparison of hydraulic geometry between sand-and gravel-bed rivers in relation to channel pattern discrimination. Earth Surface Processes and Landforms: The Journal of the British Geomorphological Research Group, 29(5): 645-657. https://doi.org/10.1002/esp.1059

Yousefi S., Pourghasemi H. R., Hooke J., et al., 2016. Changes in morphometric meander parameters identified on the Karoon River, Iran, using remote sensing data. Geomorphology, 271: 55-64. https://doi.org/10.1016/j.geomorph.2016.07.034

Yukawa S, Watanabe T, Hara K., 2019. Bifurcation Angle Distribution in the Japanese River Network. Journal of the Physical Society of Japan 88(2): 024901. https://doi.org/10.7566/ JPSJ.88.024901

Zhang T. Y., Suen C. Y., 1984. A fast parallel algorithm for thinning digital patterns. Communications of the ACM, 27(3): 236-239.

Zhu H., Li C., Zhang L., et al., 2015. River channel extraction from SAR images by combining gray and morphological features. Circuits, Systems, and Signal Processing, 34(7): 2271-2286. https://doi.org/10.1007/s00034-014-9922-2